

## Article

# Deformation Behavior of Two-Phase Gradient Nanograined Fe<sub>95</sub>Ni<sub>5</sub> Alloys under Different Types of Loading

Aleksandr Korchuganov , Dmitriy Kryzhevich \* and Konstantin Zolnikov

Institute of Strength Physics and Materials Science of Siberian Branch of Russian Academy of Sciences, Akademicheskii 2/4, 634055 Tomsk, Russia

\* Correspondence: kryzhev@ispms.ru

**Abstract:** In this paper, we used molecular dynamics simulations to study the atomic mechanisms of phase transformations, plasticity features, and mechanical properties of two-phase Fe<sub>95</sub>Ni<sub>5</sub> (at. %) samples with a gradient nanograined structure under uniaxial deformation and shear. The simulated samples with a uniform distribution of Ni atoms are composed of fcc grains from 10 to 30 nm in size, which in turn contain bcc interlayers in the form of lamellae of various distribution and size. It was shown that uniaxial loading or shear causes the bcc-fcc phase transformation in the lamellae. In the vast majority of cases, phase transformations are initiated at the junction of lamellae and grain boundaries. Deformation-induced phase transformations in lamellae occur at the front of bands propagating from grain boundaries. Grains larger than ~15 nm can have several bands or regions with differently orientated fcc lattices, whose meeting results in grain fragmentation. It was found that the atomic volume increases abruptly during the bcc-fcc structural phase transformation. The Kurdjumov–Sachs orientation relation is valid between the initial bcc and formed fcc structures. It was shown that the volume fraction and spatial distribution of the bcc phase significantly affect the yield stress of the sample. The yield stress can be increased by forming the bcc phase only in large-grained layers. This behavior is associated with the fragmentation of large grains, and consequently with grain refinement, which, in accordance with the Hall–Petch relation, improves the strength of the material.

**Keywords:** gradient nanograined alloy; plastic deformation; plasticity mechanism; dislocation; stacking fault; molecular dynamics



**Citation:** Korchuganov, A.; Kryzhevich, D.; Zolnikov, K. Deformation Behavior of Two-Phase Gradient Nanograined Fe<sub>95</sub>Ni<sub>5</sub> Alloys under Different Types of Loading. *Metals* **2022**, *12*, 1492. <https://doi.org/10.3390/met12091492>

Academic Editor: John D. Clayton

Received: 10 August 2022

Accepted: 6 September 2022

Published: 9 September 2022

**Publisher's Note:** MDPI stays neutral with regard to jurisdictional claims in published maps and institutional affiliations.



**Copyright:** © 2022 by the authors. Licensee MDPI, Basel, Switzerland. This article is an open access article distributed under the terms and conditions of the Creative Commons Attribution (CC BY) license (<https://creativecommons.org/licenses/by/4.0/>).

## 1. Introduction

At present, more and more researchers, concerned with mechanisms of a simultaneous increase in strength and ductility, improvement of the fatigue limit, and decrease of friction and wear in metallic materials, are addressing the idea of designing various classes of heterogeneous and hierarchical structures. Among them are bimodal [1–3], multimodal [4,5] and gradient grained structures [6–11], harmonic structures (conglomerates of coarse grains in the nanostructured matrix) [12], two-phase materials [13,14], twinned [15–17] and lamellar structures [18], laminates [19], etc. The main principle of designing heterogeneous materials, which have very different structures, is the formation of regions with specific mechanical and strain characteristics. The interaction between such regions gives a heterogeneous material with unique combinations of physical and mechanical properties exceeding those of its individual constituent regions.

Numerous experimental data have shown that high strength and ductility of heterogeneous materials result from additional strain hardening [9,20–22]. In turn, higher strain hardening is caused by a significant increase of back stresses, which is the case with gradient nanograined metals and alloys [18,20], two-phase materials [13,14], etc. Long-range back stresses are induced by piling-up of geometrically necessary dislocations at interfaces. The emission of new dislocations by the pile-up is possible only with increasing

stress. In heterogeneous materials, the back stress is correlated with the strain gradient initiated by strain partitioning between adjacent structural elements [18,22]. The experimental data have shown that strain gradient, strain partitioning, pile-ups of geometrically necessary dislocations, and back stress play a key role in resolving the dilemma between strength and ductility of heterogeneous metallic materials [18,21–23]. The mentioned deformation properties can be controlled by adjusting the size and shape of grains and their spatial distribution, by forming phases with significantly different physical and mechanical characteristics, etc.

Considerable study is currently given to heterogeneous metallic materials with a gradient grained structure, combining high strength and fracture toughness [23–25]. The calculation results showed that a higher grain size gradient improves the strength of materials [25]. Despite the nonuniform distribution of stresses in such a sample, plastic deformation begins almost simultaneously in layers with different grain sizes. In this case, the dominant deformation mechanism in each layer depends on the grain size. For coarse-grained layers, the main plasticity mechanism is the slip of dislocations emitted by grain boundaries. Grain boundary processes, such as grain boundary sliding and/or grain rotation, are the prevailing plasticity mechanism in fine-grained layers.

Based on the experimental data, a new model was proposed for a heterogeneous two-phase material with sufficiently different strain properties in each phase [14]. According to the model, the hard phase occurs in fine grains whose volume fraction is much larger than that of coarse grains, which contain the soft phase. The calculations showed that loading causes geometrically necessary dislocations to pile up at the phase boundary and back stresses to increase in the soft phase. As a result, the soft phase is strengthened, contributing to interphase strain hardening and the overall strain hardening of the composite. Despite the above achievements, the mechanism of strain hardening in heterogeneous materials invites further investigations.

The dilemma between strength and ductility of heterogeneous metallic materials can be resolved by designing and studying samples with combined unique properties of gradient grained metals and alloys and heterogeneous two-phase nanostructures. In our work, we study atomic mechanisms of phase transformations, plasticity features, and mechanical properties of the gradient nanograined Fe<sub>95</sub>Ni<sub>5</sub> alloy, with bcc lamellae differently distributed in fcc grains, under shear, uniaxial tension, and compression.

## 2. Computational Procedure and Interatomic Potential Validation

The studies are based on molecular dynamics simulations in the LAMMPS software (version 29Mar19, Sandia National Laboratories, Livermore, CA, USA) package [26]. The interatomic interaction in the Fe-Ni system is described by a many-body potential developed within the embedded atom method [27]. The potential correctly describes the phase diagram of the Fe-Ni system, elastic moduli, and stacking fault energies in a wide range of concentrations of chemical elements. The simulated Fe<sub>95</sub>Ni<sub>5</sub> (at. %) samples with a uniform volume distribution of Ni atoms have a two-phase gradient nanograined structure. Grains with the fcc lattice contain bcc interlayers in the form of lamellae. The volume fraction of bcc interlayers in the simulated samples varies from 10 to 50%; each grain contains from 0 to 2 interlayers. Each interlayer is modeled by cutting the grain with two parallel planes, with the bcc structure being specified between them. In this case, the Nishiyama–Wasserman orientation relation is valid between the bcc and fcc phases. As for two interlayers in a grain, they are set parallel to each other, and a fcc interlayer is placed between them. The volume fraction of the bcc phase is calculated as the ratio of the number of atoms in the bcc lattice to the number of atoms in the fcc lattice, excluding atoms belonging to grain boundaries. The fraction of the bcc phase in the sample is varied by changing the thickness and number of bcc interlayers, which is realized by changing the distance between the secant parallel planes. The grain structure is modeled by partitioning the space into polyhedra using the Laguerre–Voronoi tessellation method, which, in contrast to the Voronoi tessellation, makes it possible to accurately control the grain size in samples with a gradient grained

structure. All grains in a sample have the same crystallographic direction [123] of the fcc lattice, coinciding with the texture axis of the sample (Y axis in Figure 1). The grain orientation is set by rotation around this axis by a random angle provided that the angle between adjacent grains is no less than  $30^\circ$ .

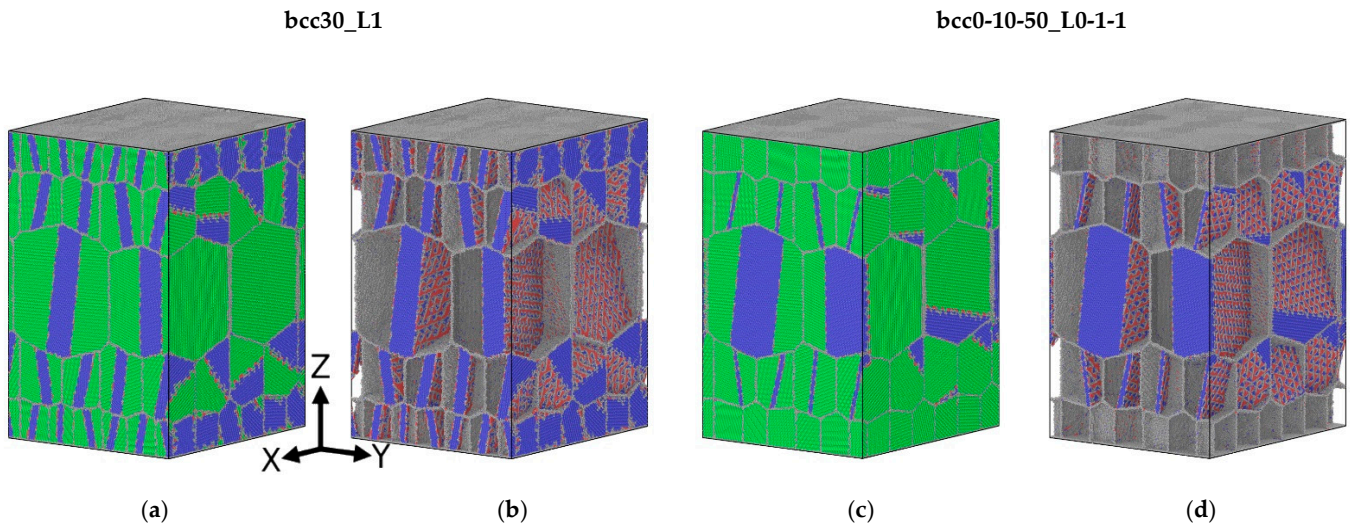


**Figure 1.** Initial structure of the simulated two-phase samples with the grain size gradient. Regions occupied by the fcc and bcc phases are highlighted in green and blue, respectively. Grain boundaries and free surfaces are gray. In (a,c), all atoms are shown. In (b,d), regions with the fcc phase are not shown.

The gradient grained structure of a sample is composed of five layers with approximately equal grains: small- (10 nm), medium- (15 nm), large- (30 nm), medium-, and small-grained layers (Figure 1) lying along the Z axis starting from the free surface. The centers of grains in layers of the same grain size are located at the sites of a conditional triangular lattice. Periodic boundary conditions are used along the X and Y axes, and the free surfaces are specified in the Z direction. The simulated samples measure  $60 \text{ nm} \times 53 \text{ nm} \times 80 \text{ nm}$  along the X, Y, and Z axes, respectively. The designations and characteristics of the simulated samples are given in Table 1.

**Table 1.** Designations and characteristics of the simulated samples.

Sample Designations	Fraction of the bcc Phase in Small-, Medium- and Large-Grained Layers, %	The Number of Interlayers in Small-, Medium- and Large-Grained Layers
bcc0_L0	0/0/0	0/0/0
bcc30_L1	30/30/30	1/1/1
bcc50_L1	50/50/50	1/1/1
bcc50_L2	50/50/50	2/2/2
bcc0-0-30_L0-0-1	0/0/30	0/0/1
bcc0-10-50_L0-1-1	0/10/50	0/0/1

Loading of samples by uniaxial uniform tension or compression along the Y axis at a constant velocity of 5 m/s is specified by scaling the Y coordinates of atoms and the linear size of samples. For shear loading, rigid grips with the thickness of four lattice parameters are set on the free surfaces, which move in the opposite directions along the Y axis at a velocity of 2.5 m/s. A thermostat and barostat are used in the calculations to keep a temperature of 300 K and zero stress along the X axis during relaxation and mechanical loading.

Structural defects in the simulated samples are searched for and identified on the basis of common neighbor analysis [28], which locally determines the crystal lattice symmetry

around each atom. Thus, intrinsic stacking faults in the fcc lattice are represented as two neighboring planes of atoms with the hcp nearest neighbor symmetry. Atoms at grain boundaries, interphase boundaries, and in dislocation cores are identified as atoms with uncertain nearest neighbor symmetry. The atomic volume of each atom is calculated as the volume of the corresponding Voronoi polyhedron. The structure of the samples is visualized using the OVITO package (version 3.0, OVITO GmbH, Darmstadt, Germany) [29].

Our test simulations with chosen interatomic potential [27] showed that the stability of the bcc lattice in the Fe-Ni system depends not only on the Ni concentration, but also on the grain size. At room temperature, the bcc phase in the simulated single crystal is stable as the Ni concentration increases to 25%. In nanocrystalline samples with the Ni concentration more than 10%, the bcc-fcc transformation occurs under the influence of grain boundaries. Such behavior of the material is consistent with the results [30] derived, both experimentally and thermodynamically, for the Fe<sub>88</sub>Ni<sub>12</sub> alloy powder and report an increase in the stability of the fcc phase with decreasing grain size.

### 3. Results and Discussion

#### 3.1. Uniaxial Tension

General information on the mechanical response of a material to loading can be received from the analysis of the stress–strain dependence. Figure 2 plots such dependence for the bcc30\_L1 sample. From the curve it is seen that the sample is elastically deformed up to the tensile strain of ~2.50%. Structural analysis shows that a flatter slope of the curve in the strain range from 2.50 to 3.25% is due to the activation of such processes as grain boundary migration, nucleation, and propagation of stacking faults in grains. The most intensive rearrangement of the sample structure occurs at the strain 3.25–4.25%, which is associated not only with the active generation of various defects, but also with bcc-fcc/hcp structural phase transformations within lamellae, which leads to an abrupt drop in the curve. At higher strains, plastic flow is established in the sample.

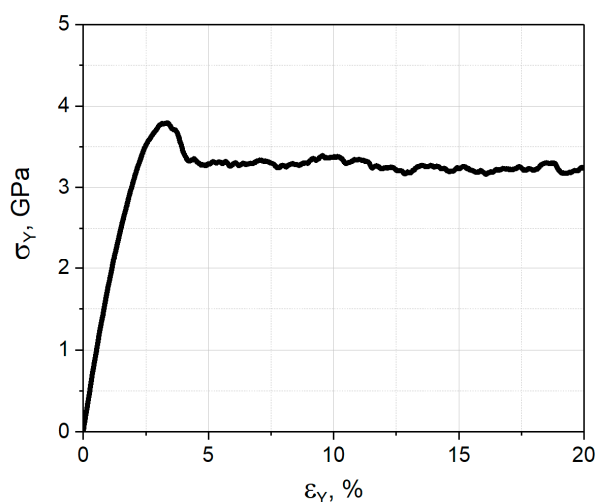


**Figure 2.** Stress–strain dependence for the bcc30\_L1 sample in tension.

The calculation results show that, in the bcc30\_L1 sample, structural phase transformations in lamellae are initiated either in the region of their contact with grain boundaries or at the phase interface within the grain. In this case, phase transformations proceed differently in different layers. For example, in the large-grained layer, the bcc lattice of lamellae begins to transform into the fcc lattice at the tensile strain of ~3.25%. Phase transformations in this layer appear as the generation and propagation of bands. Figure 3 shows the evolution of an fcc band with numerous stacking faults and hcp regions in a lamella of the large grain. During propagation, the fcc/hcp band uniformly widens throughout its length until it reaches the opposite grain boundary (Figure 3a,b). Under further loading, the phase

transformation develops due to the band expansion in both directions by almost flat fronts until it occupies most of the lamella (Figure 3c). Along with the band expansion, another front of the bcc-fcc transformation is initiated at the junction of the lamella with the lower grain boundary (Figure 3d). When the fronts of structural phase transformations from different regions meet, the lamella is fragmented into two parts, being misoriented by several degrees relative to each other. The boundary between these fragments presents a wall of partial dislocations. Its active migration and change is observed during subsequent deformations. As can be seen from the XY cross-sections of the lamella, the transformation of the bcc lattice leads to the formation of an fcc/hcp subgrain with the boundary composed of partial dislocations. The reorientation of the subgrain lattice relative to the surrounding fcc grain is shown in Figure 3c by a dotted line.

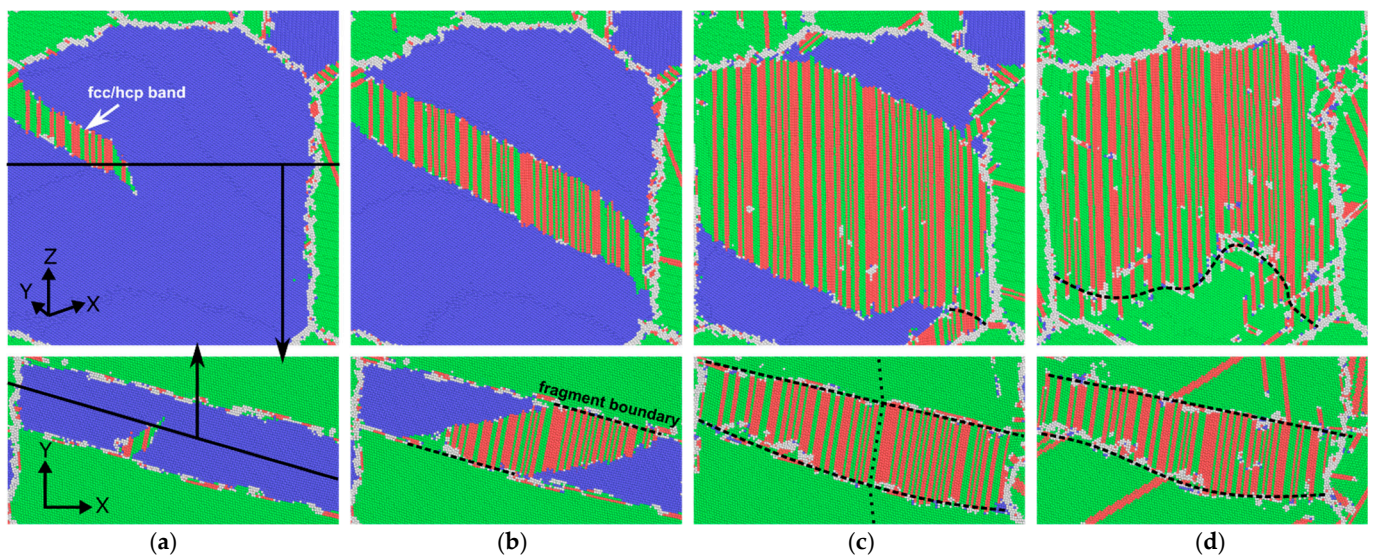


**Figure 3.** Cross-sections of a bcc lamella by the  $(\bar{1}10)$  plane parallel to the bcc/fcc interface (upper row) and by the XY plane (lower row) at the strains 3.25 (a), 3.50 (b), 5.50 (c), and 15.25% (d). Atoms with bcc, fcc, hcp and uncertain nearest neighbor symmetry are highlighted in blue, green, red, and light grey, respectively. Traces of the sectional planes are marked off by the black solid lines. Grain reorientation is shown as a dotted line and fragment boundaries as dashed lines.

A somewhat different scenario is observed in a lamella of the adjacent large grain. Structural phase transformations in this lamella are generated at the phase interface within the grain and are caused by the phase transformation in the bcc lamella of the neighboring grain, which is accompanied by intense emission of dislocations from the boundary between the grains. These dislocations arrive at the bcc/fcc interface, considerably changing its shape and forming a stress concentrator responsible for the bcc-fcc/hcp transformation in the lamellae (Figure 4a,b). Further structural phase rearrangements in this lamella proceed according to the same scenario as in the previous lamella (Figure 4c,d).

In the process of deformation, two bands of structural phase transformations with the same or different orientations of the fcc lattice can simultaneously form in a lamella of the large grain. First, the bands propagate from one grain boundary to another and then widen within the lamella. The number of bands, their nucleation sites, and growth directions in the grain are determined by structural features of the grain boundary region brought into contact with the lamellae.

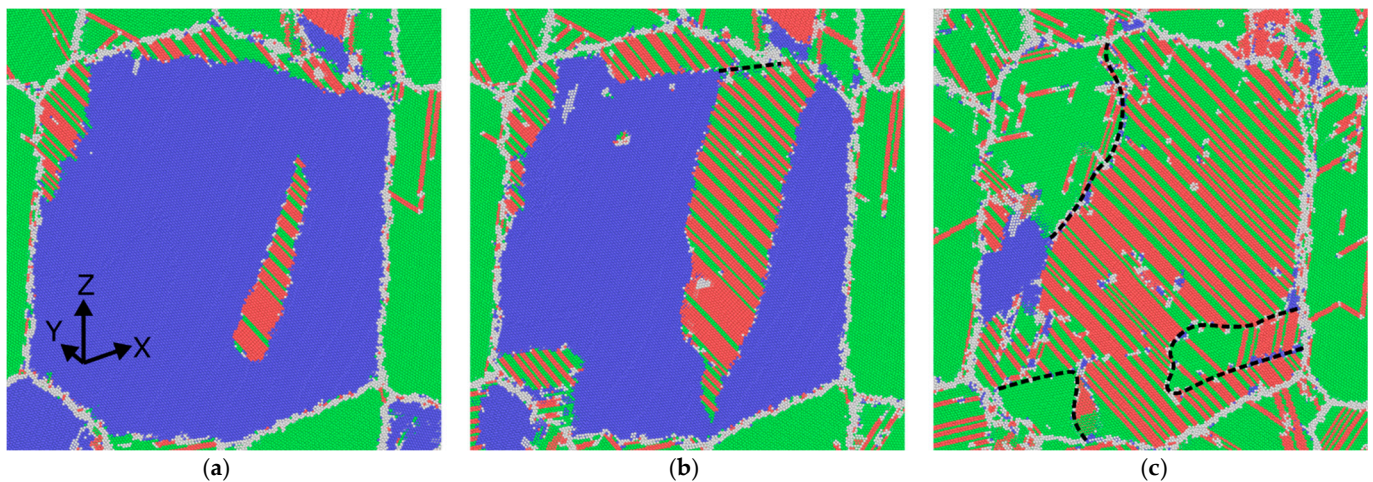


**Figure 4.** Cross-sections of a bcc lamella by the  $(\bar{1}10)$  plane parallel to the bcc/fcc interface in the large-grained layer at the strains 4.75 (a), 6.25 (b), and 8.75% (c). Atoms with bcc, fcc, hcp and uncertain nearest neighbor symmetry are shown in blue, green, red, and light grey, respectively. Fragment boundaries are marked off by dashed lines.

The generation and propagation of fcc and hcp bands is, as a rule, accompanied by migration of the grain boundary region that comes into contact with the lamella. It was found that the subgrain boundaries composed of phase interfaces experience significantly larger displacements during deformation than the grain boundaries. The higher mobility of subgrain boundaries is associated with their structure: they have the misorientation angle at about  $15^\circ$ , refer to tilt boundaries, and are formed by partial Shockley dislocations. The mechanism of the subgrain boundary migration consists in the coordinated motion of dislocations forming the boundary along their slip planes.

In the medium-grained layer, the process of generation and development of structural phase transformations is closely similar to that in large grains. Phase transformations in lamellae are also initiated at the junction with grain boundaries and propagate in the form of one or two bands (Figure 5).

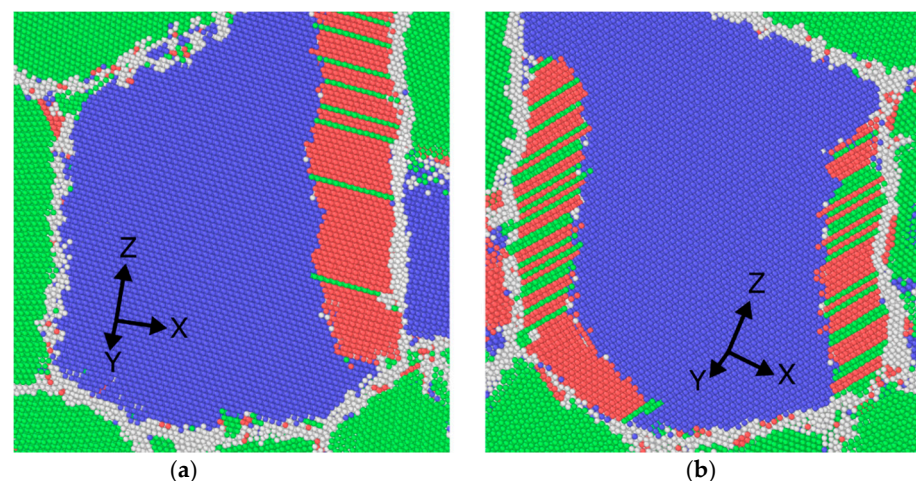


**Figure 5.** Cross-sections of a bcc lamellae by the  $(\bar{1}10)$  plane parallel to the bcc/fcc interface in two different medium grains with one (a) and two (b) fcc/hcp bands at the strain 3.00%. Atoms with bcc, fcc, hcp and uncertain nearest neighbor symmetry are shown in blue, green, red, and light grey, respectively.

In the small-grained layer, structural phase transformations in lamellae are realized through the propagation of one band generated at the grain boundary or near the free

surface. Phase transformations in lamellae of small grains can start, develop, and end on various deformation intervals. Whereas the structure of some lamellae is completely transformed into the fcc lattice, other grains retain the initial bcc lamellae (Figure 6).

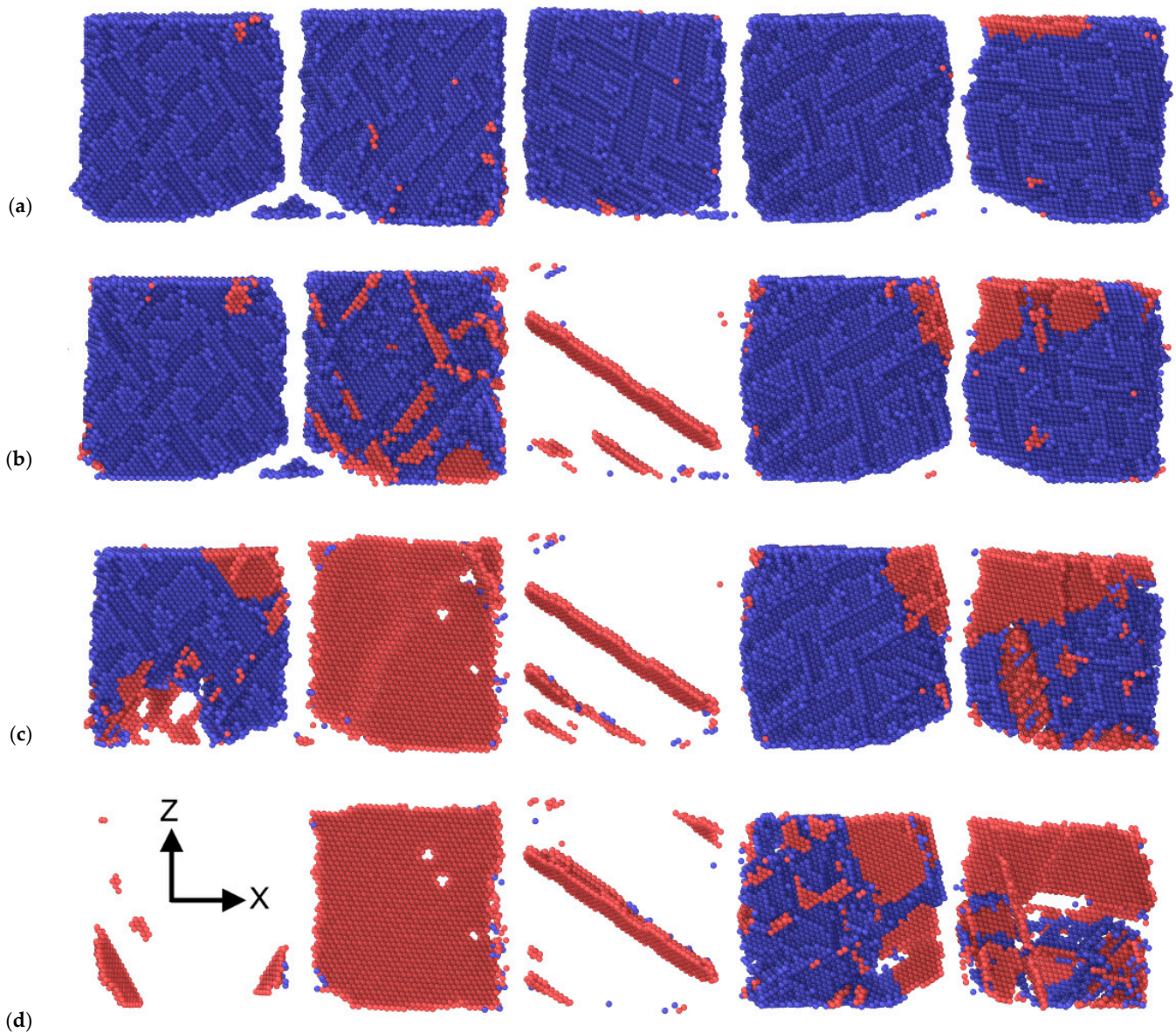


**Figure 6.** Cross-sections of a small-grained layer by the XZ plane at the strains: 1.75 (a), 3.00 (b), 4.25 (c), and 6.75% (d). Atoms with bcc and hcp nearest neighbor symmetry are highlighted in blue and red, respectively. The rest atoms are not shown.

It was found that the density of the formed defects depends significantly on the grain size (grain boundary density) in the sample. The smaller the grain size, the lower the density of structural defects formed in it. Small-grained layers are characterized by the lowest density of structural defects throughout the process of sample deformation. This deformation feature of different material layers is explained by the fact that grain boundaries act as effective sinks of various defects.

The phase transformation intensity in different layers and at different strains has its own pattern, which is illustrated in Figure 7. It can be seen that a large-grained layer corresponds to the central Z-coordinate interval 25–55 nm, two medium-grained layers are on the intervals from 12 to 25 and from 55 to 68 nm, and small-grained layers occupy the edge intervals. Figure 7 shows that the fraction of the bcc phase in the large- and

medium-grained layers changes rather non-uniformly along the Z axis during loading. The comparison of the bcc phase fractions in different layers during loading shows that the transformation intensity depends on the grain size. The maximum intensity of structural phase transformations is observed in the small-grained layer, and the minimum intensity in the large-grained layer.

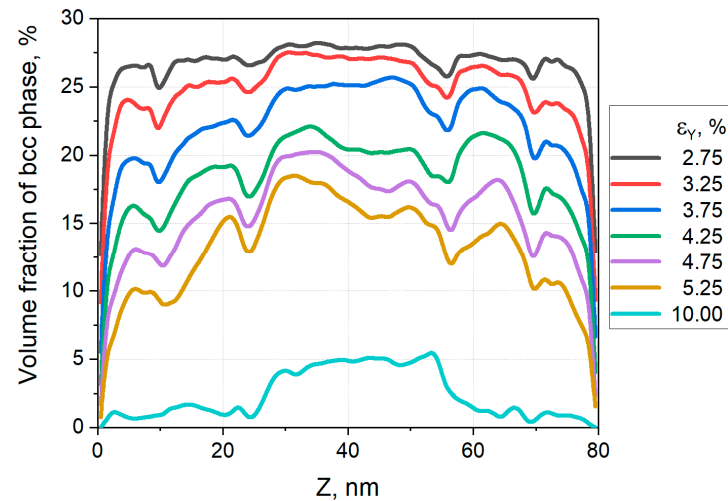


**Figure 7.** Z-axis distribution of the volume fraction of the bcc phase for different tensile strains of the bcc30\_L1 sample.

### 3.2. Uniaxial Compression

With reference to Figure 8, it can be seen that structural transformations in lamellae of the bcc30\_L1 sample under uniaxial compression cause an abrupt stress drop at the strain at  $\sim 3.75\%$ . In this case, the transition to the plastic flow stage occupies a longer strain interval as compared to uniaxial tension.

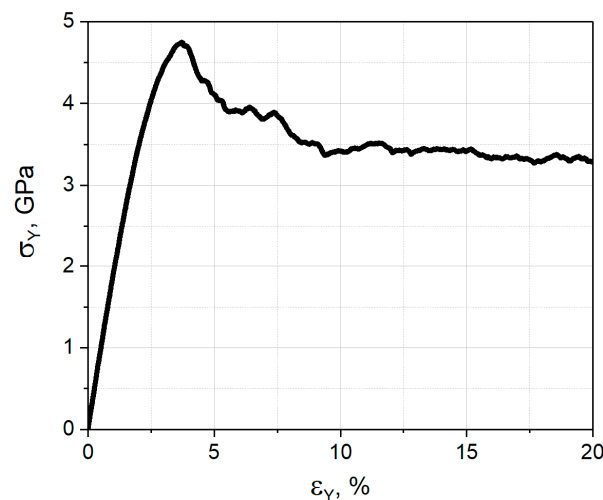


**Figure 8.** Stress–strain dependence for the bcc30\_L1 sample under compression.

The calculation results show that the bcc-fcc/hcp phase transformation in lamellae of large grains is initiated almost simultaneously in different contact regions of the lamellae and grain boundaries. This results in the formation of differently oriented fcc bands in the lamellae (Figure 9a). Several such bands initiated in the same lamella expand until they meet each other, causing fragmentation (Figure 9b). The phase transformation front velocity is much higher in the direction parallel to the phase interface than that in the direction normal to it. However, deformation-induced structural transformation in the lamellae of large grains could proceed without fragmentation. This is because most lamella have one

phase transformation front or several fronts providing equally oriented fcc lattices. The phase transformation of a lamella with the single front ends much faster than that with two or more fronts.

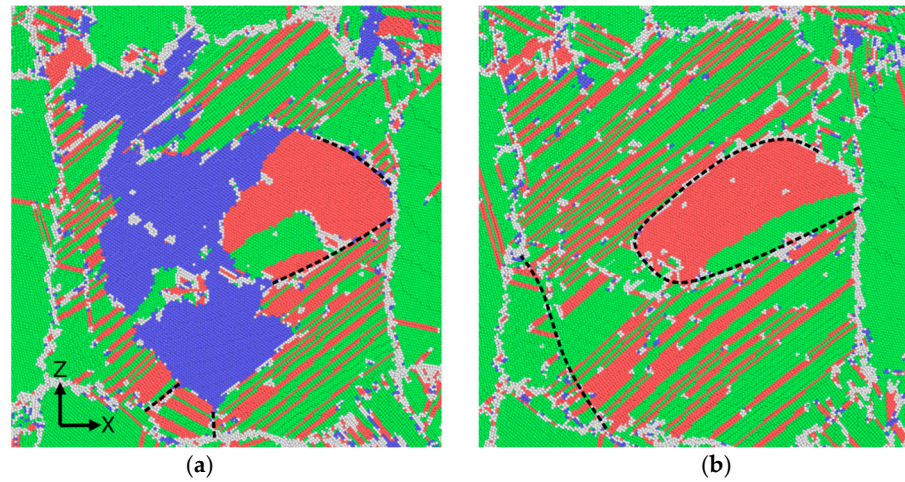


**Figure 9.** Cross-section of a lamella of the large grain by the bcc  $(\bar{1}10)$  plane parallel to the bcc/fcc interface at the compressive strains 15.00 (a) and 20.00% (b). Atoms with bcc, fcc, hcp and uncertain nearest neighbor symmetry are shown in blue, green, red, and light gray, respectively. Fragment boundaries are marked off by dashed lines.

On the entire strain interval, the intensity of structural phase transformations in the medium-grained layer is significantly lower than that in the large-grained layer. The bcc phase is retained in a significant volume of the lamellae of medium grains at 20% of strain. At the same time, some lamellae in medium grains undergo fragmentation into regions with differently orientated fcc lattices (Figure 10).

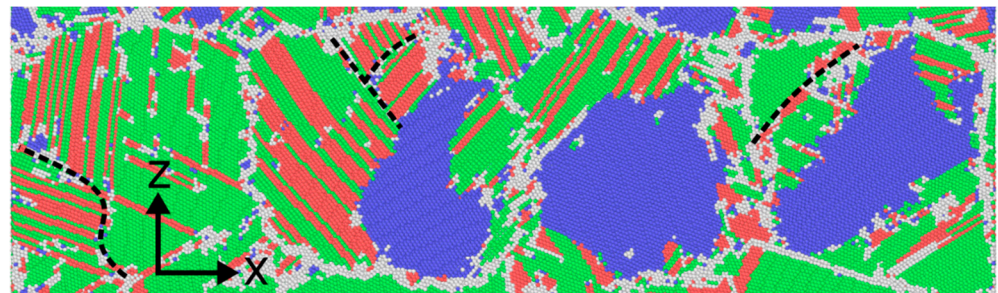


**Figure 10.** Cross-section of the medium-grained layer by the XZ plane at the strain 9.25%. Atoms with bcc, fcc, hcp and uncertain nearest neighbor symmetry are shown in blue, green, red, and light gray, respectively. Fragment boundaries are marked off by dashed lines.

In the small-grained layer, the bcc-fcc transformation in lamellae begins at lower strains than in the medium-grained layer. This could be due to the contact of small grains with the free surface. The generation and development of structural phase transformations in different lamellae of small grains occurs on significantly different strain intervals. Whereas the structure of some lamellae is completely transformed into the fcc one, the phase transformation just starts in other lamellae (Figure 11).

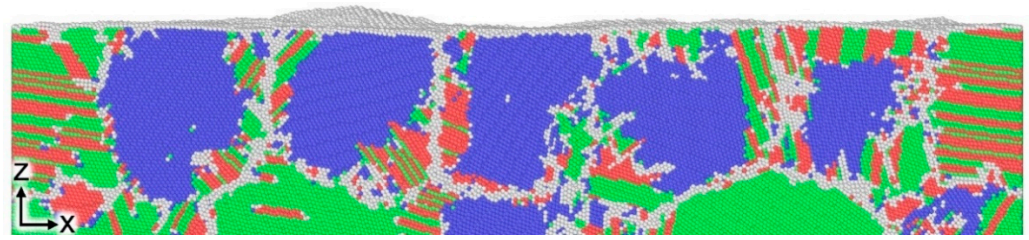


**Figure 11.** Cross-section of a small-grained layer by the XZ plane at the strain 7.00%. Atoms with bcc, fcc, hcp, and uncertain nearest neighbor symmetry are highlighted in blue, green, red, and light gray, respectively.

The analysis of the simulation results shows that the phase transformation intensity in different layers of the sample changes significantly during deformation. Thus, up to approximately 7.50% compression, the maximum phase transformation intensity is observed in the small-grained layers. At higher strains, the most intensive phase transformations occur in the large-grained layer (Figure 12). The bcc structure in the large-grained layer is almost completely transformed into the fcc structure at the 20% compression.

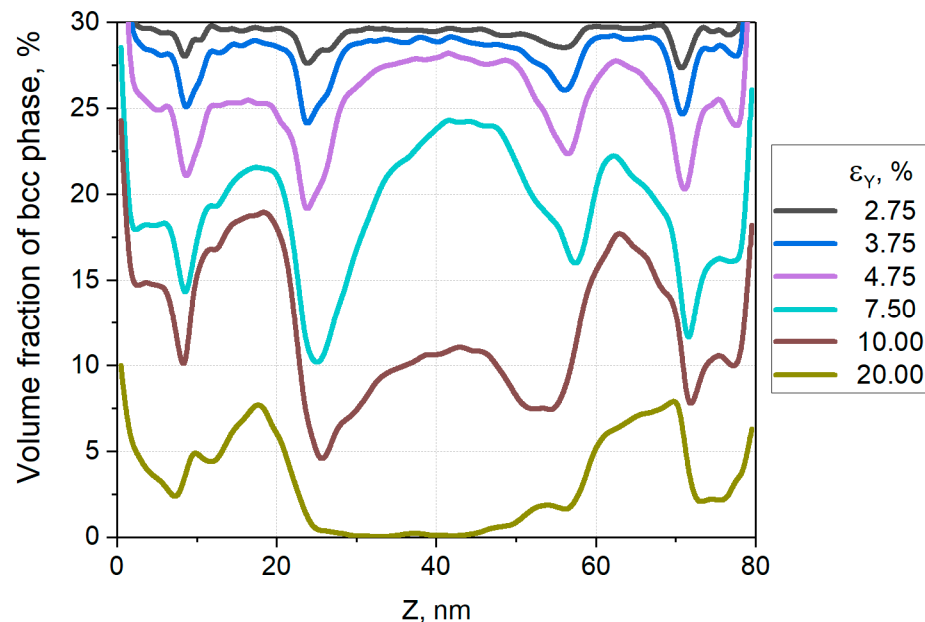


**Figure 12.** Z-axial distribution of the volume fraction of the bcc phase for different compressive strains of the bcc30\_L1 sample.

Under compression, the volume fraction of the bcc phase is found to decrease more slowly as compared with the sample under tension. In addition, a large volume of the bcc phase is retained in the sample up to the 20% compression, while, under tension, the bcc lattice is almost completely transformed into the fcc/hcp one up to the ~15% strain.

### 3.3. Shear

The deformation behavior of samples under shear loading differs markedly from the behavior under uniaxial tension and compression, which is illustrated by the stress–strain curve in Figure 13. No stress drop associated with intensive phase transformations and defect generation is observed at the critical strain. Phase transformations in the sample begin at the shear strain 0.0125, changing the slope of the curve (Figure 13). In the strain range from 0.0125 to 0.0500, the phase transformation intensity in lamellae, especially in the medium-grained layer, increases, which is evident from Figure 14. However, even more intensive phase transformations in lamellae occur starting from the strain 0.0500. The almost linear portion correspondingly gives way to a much slowly increasing portion of the

curve in Figure 13. The greater the distance between the curves in Figure 14 plotted at equal strain intervals, the higher the phase transformation intensity in the corresponding sample layer. In the strain range from 0.0500 to 0.1125, the maximum phase transformation intensity is observed in the medium-grained layers. At higher strains, phase transformations become more intensive in the large-grained layer. In general, up to the strain 0.1500, the slope of the curve in Figure 13 correlates well with the phase transformation intensity throughout the sample.

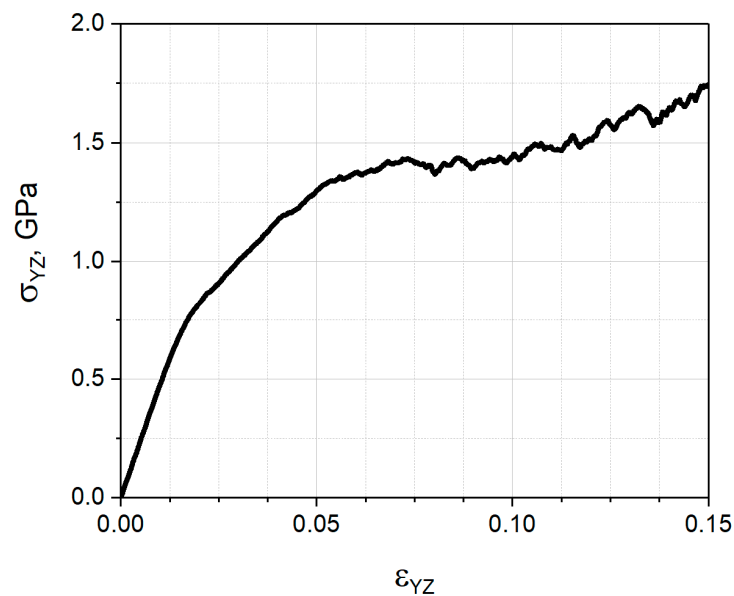


**Figure 13.** Stress–strain dependence for the bcc30\_L1 sample under shear.

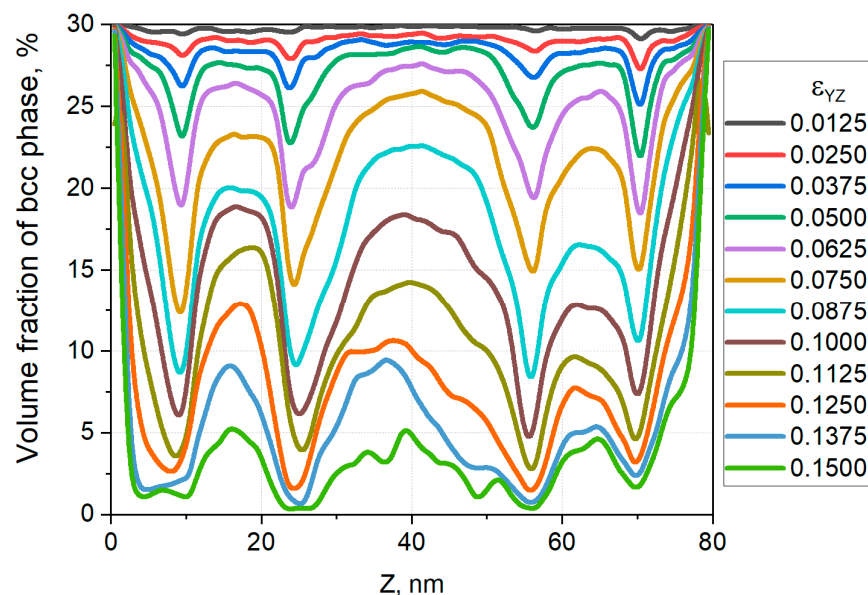


**Figure 14.** Z-axial distribution of the volume fraction of the bcc phase for different compressive strains of the bcc30\_L1 sample.

A distinctive feature of the deformation behavior of samples under shear loading is twinning during the phase transformation in most lamellae of large grains. Before loading, the phase interface between the grain and the lamella presents a thin layer consisting of 2–3 atomic planes with alternating bcc, fcc, and uncertainly structured regions (Figure 15a), which are formed by the periodic arrangement of the misfit dislocation network between the fcc and bcc lattices. Under shear loading, these dislocations begin to move, and, as the

bcc structure of the lamella transforms into the fcc structure reoriented relative to the parent grain, a twin boundary is formed at the interface. The position of the phase transformation front in the lamella during loading is shown in Figure 15b,c. It can be seen that phase transformations generate in separate regions at the interface (Figure 15b) and straighten out during propagation into the lamella (Figure 15c).

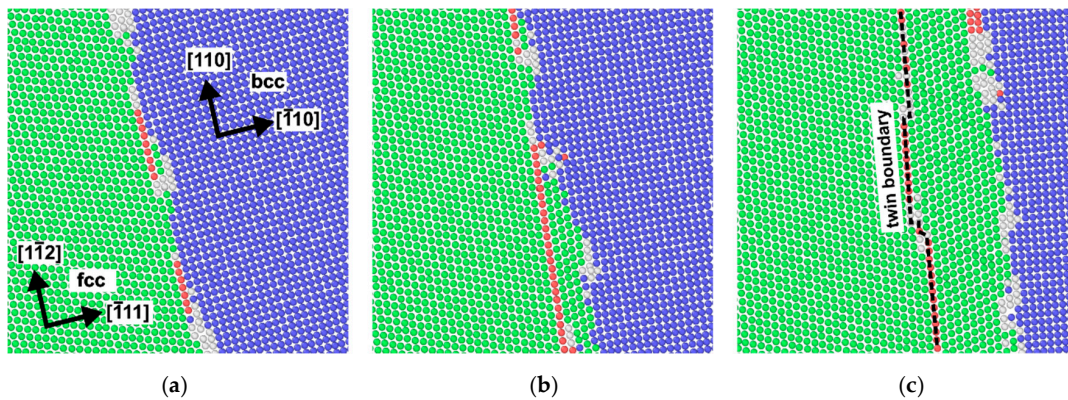


**Figure 15.** Twinning in the lamella of a large grain during shear. Cross-section of the structure by the fcc (110) plane at different shear strains: 0.000 (a), 0.065 (b), and 0.088 (c). Atoms with bcc, fcc, hcp, and uncertain neighbor symmetry are shown in blue, green, red, and light gray, respectively.

### 3.4. Atomic Mechanism of the bcc-fcc/hcp Structural Phase Transformation

Atomic mechanisms of the bcc-fcc and bcc-hcp phase transformations are studied based on the analysis of structural rearrangements in the vicinity of atoms A and B, shown by arrows in Figure 16 in a lamella of the large grain during tension of the bcc30\_L1 sample. Investigation is given to changes in the atomic volume of atoms A and B, the magnitude and direction of displacements of their neighbors in the bcc {110} planes, and the angle  $\alpha$  between adjacent  $\langle 111 \rangle$  directions in the bcc {110} planes (Figure 17). It is clearly seen (black curve) that the atomic volume increases abruptly during the phase transformation. This behavior is in good agreement with the previous experimental and simulation data [31,32], which show that the generation of structural defects and phase transformations are always accompanied by the formation of an excess atomic volume. The volume of the Voronoi cell for atom A increases by  $\sim 2.7\%$  during the bcc-fcc transformation. The angle  $\alpha$  decreases from about  $70^\circ$  to  $62^\circ$ , which is typical for the bcc-fcc lattice transformation [33].

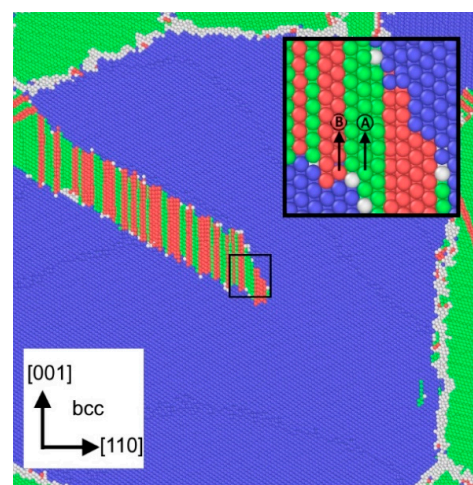


**Figure 16.** Cross-section of a lamella of the large grain by the bcc ( $\bar{1}10$ ) plane at the strain 4.20%. Atoms with bcc, fcc, hcp, and uncertain nearest neighbor symmetry are shown in blue, green, red, and light gray, respectively.

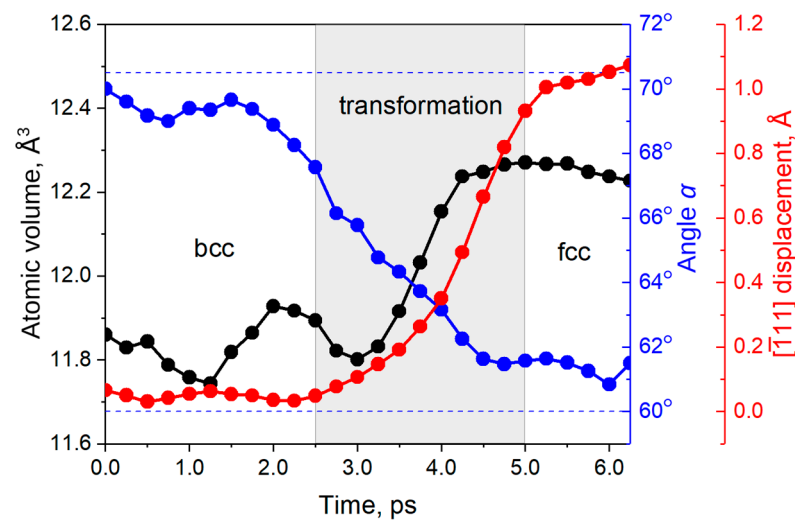


**Figure 17.** Time dependences of the Voronoi cell volume, angle  $\alpha$  between adjacent  $\langle 111 \rangle$  directions in the bcc  $\{110\}$  planes, and relative displacement of two adjacent bcc  $\{110\}$  planes in the  $[\bar{1}11]$  direction for atom A. The time axis originates at the strain 4.10%.

Atomic mechanisms of the bcc-fcc phase transformation are revealed from the analysis of changes in the magnitude and direction of displacement of atomic cells during sample loading. The structure of three bcc  $\{110\}$  atomic planes and the considered atomic cell at different time instants is displayed in Figure 18. Red solid lines connect the cell atoms in plane I, and black solid lines connect the cell atoms in plane III. Phase transformations cause the relative displacement of these cells in the bcc  $\langle 111 \rangle$  direction by  $\sim 1.0$  Å. The direction of displacement of the atomic cells is very close to the tension direction of the sample (Figure 16). The dynamics of relative displacement of these cells is shown by the red curve in Figure 17. The time interval from 2.5 to 5.0 ps is characterized by a simultaneous significant change in the studied characteristics, and corresponds to the beginning and end of structural rearrangements of the nearest neighbors for the considered atoms.

The Kurdjumov–Sachs orientation relation is valid between the formed fcc structure and the initial bcc lattice:

$$\begin{aligned} \{110\}_{\text{bcc}} \parallel \{111\}_{\text{fcc}}; \\ \langle 111 \rangle_{\text{bcc}} \parallel \langle 110 \rangle_{\text{fcc}}. \end{aligned}$$

The cross-section shown in Figure 16 reveals the formation of hcp regions and stacking faults at the front of the structural transformation band. The mechanism of formation of the hcp phase and stacking faults is studied through mutual displacements of atoms in a cell located in the three bcc  $\{110\}$  atomic planes around atom B (Figure 19). The analysis shows that the bcc-hcp transformation occurs mainly due to displacements of atoms of the bcc  $\{110\}$  planes in the  $\langle 110 \rangle$  direction. Relative displacements of planes I–III are pronounced on different projections in Figure 19. It was found that, during the phase transformation, the atoms of plane II experience the maximum displacement relative to the neighboring planes. In addition, the phase transformation is accompanied by the cell deformation, in particular, the angle  $\alpha$  decreases from approximately  $70$  to  $58^\circ$ . Changes in the Voronoi cell volume for atom B, displacements of plane II atoms, and angle  $\alpha$  are shown in Figure 20. It can be seen that these characteristics behave similarly to those during the bcc-fcc transformation. The structural analysis at the phase transformation front shows that the formation of hcp bands with the thickness of more than two layers in the fcc  $\langle 111 \rangle$  direction is due to the simultaneous passage of two or more stacking faults in the neighboring fcc  $\{111\}$  planes.

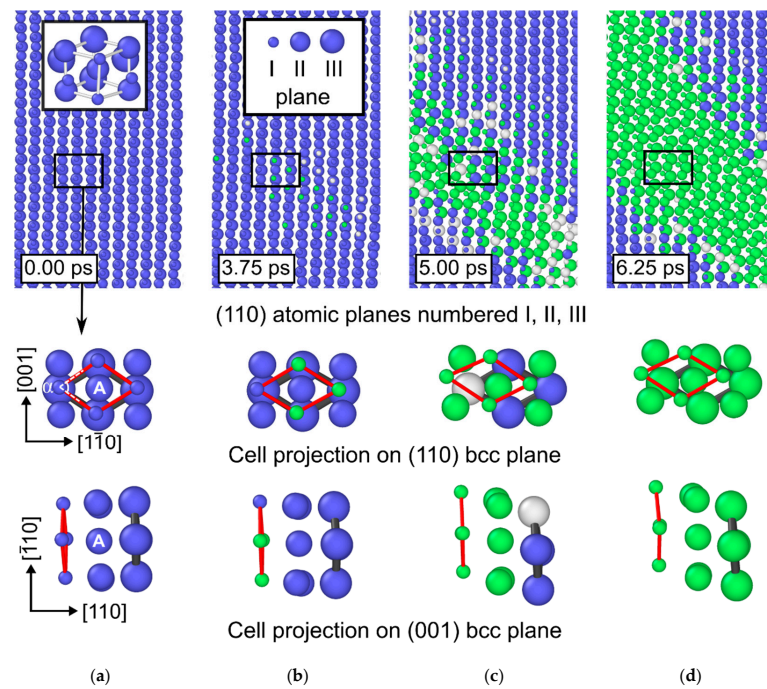


**Figure 18.** Three adjacent (110) planes (upper row) and projections of the analyzed cell around atom A onto the (110) plane (middle row) and the (001) plane (lower row) at the time instants 0.00 (a), 3.75 (b), 5.00 (c), and 6.25 ps (d). The size of atoms corresponds to their position in the bcc (110) planes numbered I, II, and III. Atoms with bcc, fcc, and uncertain nearest neighbor symmetry are shown in blue, green, and gray, respectively. The inset in (a) exhibits the initial 3D view of the analyzed atomic cell, where gray solid lines represent the edges of the bcc Bravais cell.

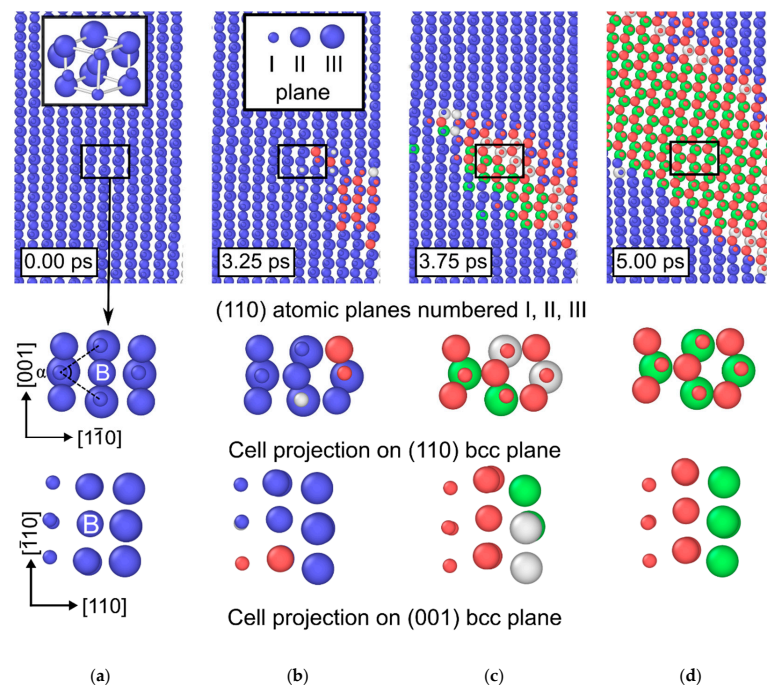


**Figure 19.** Three adjacent (110) planes (upper row) and projections of the analyzed cell around atom B onto the (110) plane (middle row) and the (001) plane (lower row) at the time instants 0.00 (a), 3.25 (b), 3.75 (c), and 5.00 ps (d). The size of atoms corresponds to their position in the bcc (110) planes numbered I, II, and III. Atoms with bcc, fcc, and uncertain nearest neighbor symmetry are shown in blue, green, and gray, respectively. The inset in (a) exhibits the initial 3D view of the analyzed atomic cell, where gray solid lines represent the edges of the bcc Bravais cell.

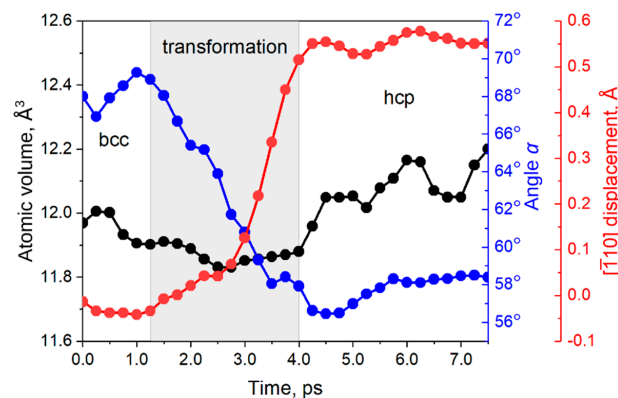


**Figure 20.** Time dependences of the Voronoi cell volume, angle  $\alpha$  between adjacent  $\langle 111 \rangle$  directions in the bcc  $\{110\}$  planes, and relative displacement of plane II in the bcc  $[\bar{1}10]$  direction for atom B. The time axis originates at the strain 4.10%.

As in the case of tension, the bcc-fcc/hcp structural phase transformations in a sample under compression are realized according to the Kurdjumov–Sachs scheme. In both cases, the displacements of the bcc  $\{110\}$  planes are close to the tension direction and the normal to the compression direction.

### 3.5. The Role of the bcc Phase Distribution in the Structural and Mechanical Response of the Simulated Samples

The performed calculations reveal significant differences in the processes of phase transformation and plastic deformation in layers with different grain sizes. This suggests that strength characteristics of the material can be controlled by varying the volume fraction and distribution of bcc lamellae in different layers. Our calculations show that bcc lamellae decrease the yield stress, when introduced into nanocrystalline samples with the grain size 10 nm, and increase it, when introduced into samples with the grain size 15 and 30 nm. Such behavior of nanocrystalline samples is explained by the formation of subgrains within grains due to the bcc-fcc phase transformation in lamellae. In a large-grained sample, the phase transformation results in the formation of fragments larger than 10 nm, which increases strength characteristics of the newly formed structure. If grains are small enough, they are fragmented into subgrains smaller than 10 nm, which, according to the inverse Hall–Petch effect, reduces the strength of the material [34]. From the calculations, it was found that nanocrystalline samples with the grain size 15 nm and 30 nm have maximum strength characteristics at the 10% and 50% volume fraction of bcc lamellae, respectively. These data were used to build sample bcc0-10-50\_L0-1-1, in which lamellae of optimum size were introduced only into large- and medium-grained layers. The calculation results on the deformation behavior of the samples presented in Table 1 report that the maximum yield stresses are exhibited by samples without bcc lamellae in small-grained layers. The calculation results for the simulated samples are plotted in Figure 21. The minimum strength is found in a sample whose grains contain two bcc lamellae with the total volume fraction 50%.

The physical nature of strength characteristics is revealed by a comparative analysis of structures of deformed samples that initially had 50% of bcc lamellae in large grains and different fractions in the other layers.

Cross-sections of different layers of the simulated samples are shown in Figure 22. Small-grained layers of the samples have a qualitatively similar structure. Differences become evident in medium-grained layers and are significantly enhanced in large-grained layers. This is due to the fact that thicker lamellae in the bcc50\_L1 sample (middle column in Figure 22) are transformed into subgrains, causing grain fragmentation. Thinner lamellae of the bcc50\_L2 sample (right column in Figure 22) in tension are transformed in such a way that their structure coincides with the fcc lattice of the host grain. Medium grains of the bcc0-10-50\_L0-1-1 sample strained to 20% contain no subgrains that could be formed by bcc interlayers (left column in Figure 22). The structure of thinner interlayers occupying

10% of the medium grains is transformed into the fcc lattice similar to that of the parent grains, thus increasing the ductility and retaining the strength of the bcc0-10-50\_L0-1-1 sample. Thicker interlayers occupying 50% of the medium grains in the bcc50\_L1 sample are fragmented into small subgrains, thus making them weaker as compared with the initial medium grains.

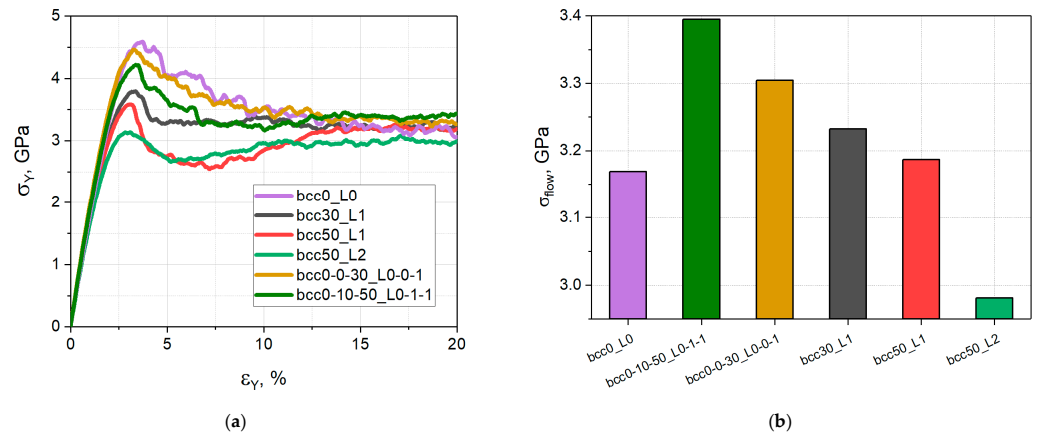


**Figure 21.** Stress–strain dependence (a) and yield stress in the strain range 17.5–20% (b) for different samples under tension.

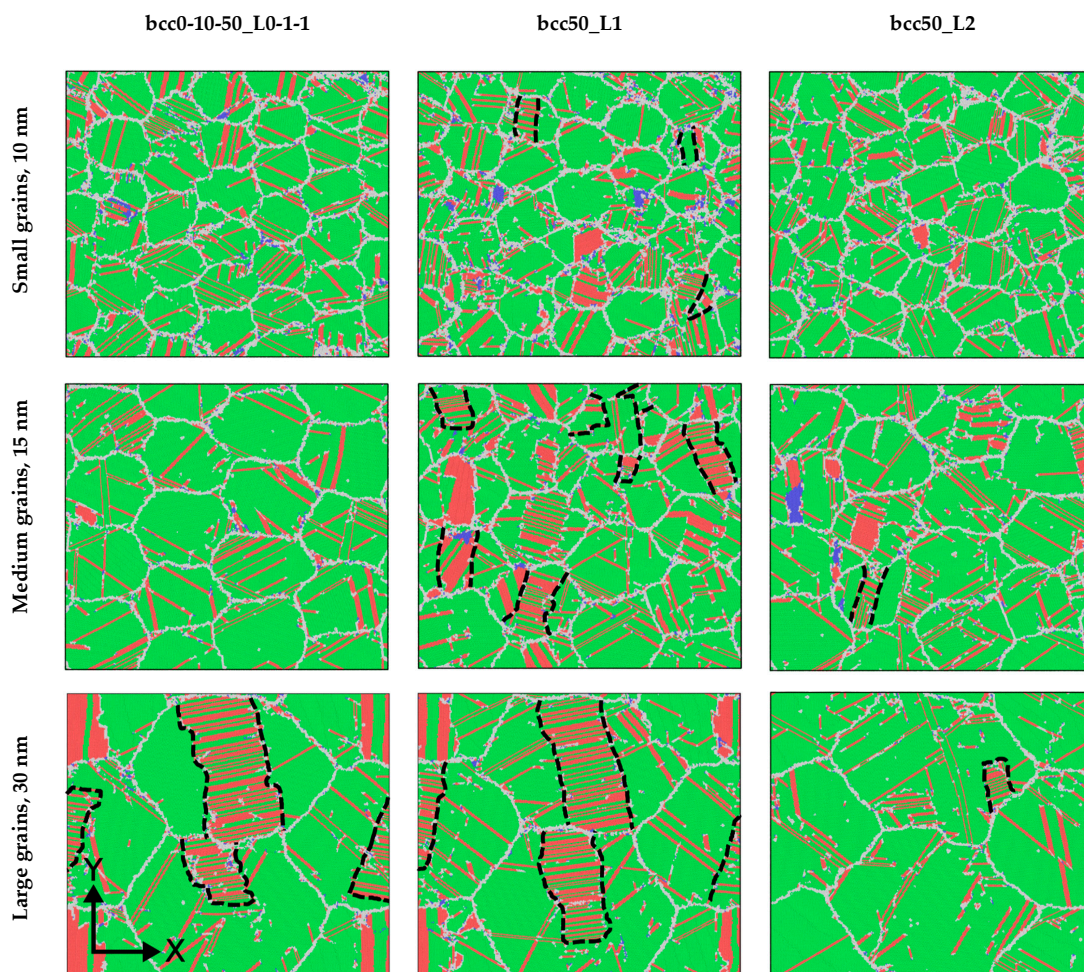


**Figure 22.** XY cross-sections of different layers of samples with differently distributed initial bcc phases stretched to 20.00%. Atoms with bcc, hcp, fcc, and uncertain nearest neighbor symmetry are shown in blue, red, green, and gray. Fragment boundaries are marked off by dashed lines.

#### 4. Conclusions

The calculation results showed that uniaxial deformation or shear causes the bcc-fcc/hcp phase transformation in lamellae of two-phase gradient nanograined Fe<sub>95</sub>Ni<sub>5</sub> samples. In uniaxial tension, phase transformation bands, at whose front the bcc structure is transformed into the fcc/hcp one, are generated in the region of contact of lamellae with grain boundaries in large and medium grains. Bands propagate and widen within the lamellae. Much less often, bands in the large-grained layer generate at the phase interface. The meeting of the band fronts with differently orientated fcc lattices leads to fragmentation of the lamella. The bcc-fcc/hcp transformation can change the phase interface into a low-angle grain boundary, thus causing fragmentation of the grain containing this lamella. In a medium-grained layer, phase transformations always generate at the junction of lamellae with grain boundaries, with the formation of one or two bands. In small grains, phase transformations result from the propagation of one band, which can originate both at the grain boundary and in the vicinity of the free surface. Phase transformations in these grains occur on different strain intervals; whereas some grains are completely transformed, other grains still have the initial structure.

In uniaxial compression, lamellae in large grains, as a rule, do not fragment, since phase transformations develop either at the front of one band or at the fronts of several bands, but the formed fcc phase has the same lattice orientation. In the entire strain range, the intensity of structural phase transformations in the medium-grained layer is significantly lower than in the large-grained layer. A significant part of the lamella volume in this layer retains the bcc phase after unloading. As in tension, phase transformations in small grains generate and develop on different strain intervals.

Under shear loading, the phase transformation leads to twinning in most lamellae of large grains.

The atomic mechanism of bcc-fcc transformations was revealed, which consists in the coordinated displacements of neighboring bcc {110} atomic planes in bcc <111> direction at the phase transformation front. In the case of bcc-hcp transformations, the central atomic plane is displaced in the bcc <110> direction to a significantly greater distance relative to the neighboring planes. The Kurdjumov–Sachs orientation relation is valid between the formed fcc structure and the initial bcc lattice. At the phase transformation front, the atomic volume increases abruptly, which is in good agreement with the available experimental and calculated data.

It was found that the volume fraction and distribution of the bcc phase in layers with different grain sizes have a significant effect on the yield stress. Maximum yield stresses were found in samples without bcc lamellae in small-grained layers. This behavior is due to the fragmentation of large grains during the phase transformation, which increases the strength of the material in accordance with the Hall–Petch relation.

Based on the investigation results, it was revealed that the strength of two-phase gradient nanograined Fe<sub>95</sub>Ni<sub>5</sub> alloy can be significantly increased without sacrificing the ductility by adjusting the proportion of the bcc phase and its distribution in layers with different grain sizes.

**Author Contributions:** Conceptualization and methodology, A.K. and K.Z.; validation and investigation, A.K. and D.K.; writing—original draft preparation, A.K.; writing—review and editing, A.K., K.Z. and D.K.; software—D.K.; visualization, A.K.; supervision and project administration, A.K. All authors have read and agreed to the published version of the manuscript.

**Funding:** The study of the deformation behavior of samples in tension and compression was carried out at the financial support of the Russian Science Foundation (Project No. 20-79-10406). Phase transformations in samples under shear loading were investigated within the Government Statement of Work for ISPMS SB RAS (Project FWRW-2021-0002).

**Data Availability Statement:** Not applicable.

**Conflicts of Interest:** The authors declare no conflict of interest.

## References

1. Arora, H.S.; Ayyagari, A.; Saini, J.; Selvam, K.; Riyadh, S.; Pole, M.; Grewal, H.S.; Mukherjee, S. High Tensile Ductility and Strength in Dual-Phase Bimodal Steel through Stationary Friction Stir Processing. *Sci. Rep.* **2019**, *9*, 1972. [[CrossRef](#)] [[PubMed](#)]
2. Wang, Y.; Chen, M.; Zhou, F.; Ma, E. High Tensile Ductility in a Nanostructured Metal. *Nature* **2002**, *419*, 912–915. [[CrossRef](#)] [[PubMed](#)]
3. Zhang, H.; Wang, H.; Wang, J.; Rong, J.; Zha, M.; Wang, C.; Ma, P.; Jiang, Q. The Synergy Effect of Fine and Coarse Grains on Enhanced Ductility of Bimodal-Structured Mg Alloys. *J. Alloys Compd.* **2019**, *780*, 312–317. [[CrossRef](#)]
4. El-Atwani, O.; Quach, D.V.; Efe, M.; Cantwell, P.R.; Heim, B.; Schultz, B.; Stach, E.A.; Groza, J.R.; Allain, J.P. Multimodal Grain Size Distribution and High Hardness in Fine Grained Tungsten Fabricated by Spark Plasma Sintering. *Mater. Sci. Eng. A* **2011**, *528*, 5670–5677. [[CrossRef](#)]
5. Xu, T.; Wang, S.; Wang, W.; Liang, P.; Li, X.; Mitsuzaki, N.; Chen, Z. Multimodal Grain Structure and Tensile Properties of Cold-Rolled Titanium after Short-Duration Annealing. *Mater. Charact.* **2020**, *160*, 110095. [[CrossRef](#)]
6. Lu, K. Making Strong Nanomaterials Ductile with Gradients. *Science* **2014**, *345*, 1455–1456. [[CrossRef](#)]
7. Cao, S.C.; Liu, J.; Zhu, L.; Li, L.; Dao, M.; Lu, J.; Ritchie, R.O. Nature-Inspired Hierarchical Steels. *Sci. Rep.* **2018**, *8*, 5088. [[CrossRef](#)]
8. Chen, W.; You, Z.S.; Tao, N.R.; Jin, Z.H.; Lu, L. Mechanically-Induced Grain Coarsening in Gradient Nano-Grained Copper. *Acta Mater.* **2017**, *125*, 255–264. [[CrossRef](#)]
9. Cheng, Z.; Zhou, H.; Lu, Q.; Gao, H.; Lu, L. Extra Strengthening and Work Hardening in Gradient Nanotwinned Metals. *Science* **2018**, *362*, eaau1925. [[CrossRef](#)]
10. Wang, J.J.; Tao, N.R.; Lu, K. Revealing the Deformation Mechanisms of Nanograins in Gradient Nanostructured Cu and CuAl Alloys under Tension. *Acta Mater.* **2019**, *180*, 231–242. [[CrossRef](#)]
11. Cao, R.; Yu, Q.; Pan, J.; Lin, Y.; Sweet, A.; Li, Y.; Ritchie, R.O. On the Exceptional Damage-Tolerance of Gradient Metallic Materials. *Mater. Today* **2020**, *32*, 94–107. [[CrossRef](#)]
12. Zhang, Z.; Vajpai, S.K.; Orlov, D.; Ameyama, K. Improvement of Mechanical Properties in SUS304L Steel through the Control of Bimodal Microstructure Characteristics. *Mater. Sci. Eng. A* **2014**, *598*, 106–113. [[CrossRef](#)]
13. Li, Z.; Pradeep, K.G.; Deng, Y.; Raabe, D.; Tasan, C.C. Metastable High-Entropy Dual-Phase Alloys Overcome the Strength–Ductility Trade-Off. *Nature* **2016**, *534*, 227–230. [[CrossRef](#)]
14. Li, J.; Lu, W.; Chen, S.; Liu, C. Revealing Extra Strengthening and Strain Hardening in Heterogeneous Two-Phase Nanostructures. *Int. J. Plast.* **2020**, *126*, 102626. [[CrossRef](#)]
15. Sun, L.; He, X.; Lu, J. Nanotwinned and Hierarchical Nanotwinned Metals: A Review of Experimental, Computational and Theoretical Efforts. *NPJ Comput. Mater.* **2018**, *4*, 6. [[CrossRef](#)]
16. Zhang, Z.; Sheng, H.; Wang, Z.; Gludovatz, B.; Zhang, Z.; George, E.P.; Yu, Q.; Mao, S.X.; Ritchie, R.O. Dislocation Mechanisms and 3D Twin Architectures Generate Exceptional Strength–Ductility–Toughness Combination in CrCoNi Medium-Entropy Alloy. *Nat. Commun.* **2017**, *8*, 14390. [[CrossRef](#)]
17. Wei, Y.; Li, Y.; Zhu, L.; Liu, Y.; Lei, X.; Wang, G.; Wu, Y.; Mi, Z.; Liu, J.; Wang, H.; et al. Evading the Strength–Ductility Trade-off Dilemma in Steel through Gradient Hierarchical Nanotwins. *Nat. Commun.* **2014**, *5*, 3580. [[CrossRef](#)]
18. Wu, X.; Yang, M.; Yuan, F.; Wu, G.; Wei, Y.; Huang, X.; Zhu, Y. Heterogeneous Lamella Structure Unites Ultrafine-Grain Strength with Coarse-Grain Ductility. *Proc. Natl. Acad. Sci. USA* **2015**, *112*, 14501–14505. [[CrossRef](#)]
19. Wang, Y.F.; Wang, M.S.; Fang, X.T.; Guo, F.J.; Liu, H.Q.; Scattergood, R.O.; Huang, C.X.; Zhu, Y.T. Extra Strengthening in a Coarse/Ultrafine Grained Laminate: Role of Gradient Interfaces. *Int. J. Plast.* **2019**, *123*, 196–207. [[CrossRef](#)]
20. Wang, Y.; Guo, F.; He, Q.; Song, L.; Wang, M.; Huang, A.; Li, Y.; Huang, C. Synergetic Deformation-Induced Extraordinary Softening and Hardening in Gradient Copper. *Mater. Sci. Eng. A* **2019**, *752*, 217–222. [[CrossRef](#)]
21. Huang, C.X.; Wang, Y.F.; Ma, X.L.; Yin, S.; Höppel, H.W.; Göken, M.; Wu, X.L.; Gao, H.J.; Zhu, Y.T. Interface Affected Zone for Optimal Strength and Ductility in Heterogeneous Laminate. *Mater. Today* **2018**, *21*, 713–719. [[CrossRef](#)]
22. Park, H.K.; Ameyama, K.; Yoo, J.; Hwang, H.; Kim, H.S. Additional Hardening in Harmonic Structured Materials by Strain Partitioning and Back Stress. *Mater. Res. Lett.* **2018**, *6*, 261–267. [[CrossRef](#)]
23. Lee, H.H.; Yoon, J.I.; Park, H.K.; Kim, H.S. Unique Microstructure and Simultaneous Enhancements of Strength and Ductility in Gradient-Microstructured Cu Sheet Produced by Single-Roll Angular-Rolling. *Acta Mater.* **2019**, *166*, 638–649. [[CrossRef](#)]
24. Korchuganov, A.V.; Zolnikov, K.P.; Kryzhevich, D.S. The Contribution of Various Plasticity Mechanisms to the Deformation Behavior of Gradient Nanograined FeNi Alloy. *Metals* **2022**, *12*, 573. [[CrossRef](#)]
25. He, C.-Y.; Yang, X.-F.; Chen, H.; Zhang, Y.; Yuan, G.-J.; Jia, Y.-F.; Zhang, X.-C. Size-Dependent Deformation Mechanisms in Copper Gradient Nano-Grained Structure: A Molecular Dynamics Simulation. *Mater. Today Commun.* **2022**, *31*, 103198. [[CrossRef](#)]
26. Plimpton, S. Fast Parallel Algorithms for Short-Range Molecular Dynamics. *J. Comput. Phys.* **1995**, *117*, 1–19. [[CrossRef](#)]
27. Zhou, X.W.; Foster, M.E.; Sills, R.B. An Fe-Ni-Cr Embedded Atom Method Potential for Austenitic and Ferritic Systems. *J. Comput. Chem.* **2018**, *39*, 2420–2431. [[CrossRef](#)]
28. Honeycutt, J.D.; Andersen, H.C. Molecular Dynamics Study of Melting and Freezing of Small Lennard-Jones Clusters. *J. Phys. Chem.* **1987**, *91*, 4950–4963. [[CrossRef](#)]
29. Stukowski, A. Visualization and Analysis of Atomistic Simulation Data with OVITO—the Open Visualization Tool. *Model. Simul. Mat. Sci. Eng.* **2010**, *18*, 015012. [[CrossRef](#)]

30. Wang, H.; Liu, Q.; Zhang, J.; Hsu, T.Y. The Size Effect on the Phase Stability of Nanograined Fe–12Ni Powders and the Magnetic Separation of Face-Centred-Cubic-Body-Centred-Cubic Phases. *Nanotechnology* **2003**, *14*, 696–700. [[CrossRef](#)]
31. Zheng, H.; Cao, A.; Weinberger, C.R.; Huang, J.Y.; Du, K.; Wang, J.; Ma, Y.; Xia, Y.; Mao, S.X. Discrete Plasticity in Sub-10-Nm-Sized Gold Crystals. *Nat. Commun.* **2010**, *1*, 144. [[CrossRef](#)]
32. Psakhie, S.G.; Zolnikov, K.P.; Kryzhevich, D.S.; Korchuganov, A.V. Key Role of Excess Atomic Volume in Structural Rearrangements at the Front of Moving Partial Dislocations in Copper Nanocrystals. *Sci. Rep.* **2019**, *9*, 3867. [[CrossRef](#)]
33. Wang, S.J.; Wang, H.; Du, K.; Zhang, W.; Sui, M.L.; Mao, S.X. Deformation-Induced Structural Transition in Body-Centred Cubic Molybdenum. *Nat. Commun.* **2014**, *5*, 3433. [[CrossRef](#)]
34. Korchuganov, A.V.; Kryzhevich, D.S.; Chumakov, Y.A.; Grigoriev, A.S. Influence of Grain Size on the Nucleation and Development of Plasticity in Nanocrystalline FeNi Films. *IOP Conf. Ser. Mater. Sci. Eng.* **2021**, *1093*, 012012. [[CrossRef](#)]